Ferroelectric domain structures in $SrBi_2Nb_2O_9$ epitaxial thin films: Electron microscopy and phase-field simulations

Y. L. Li,[a)] L. Q. Chen, G. Asayama, and D. G. Schlom
Department of Materials Science and Engineering, The Pennsylvania State University,
University Park, Pennsylvania 16802

M. A. Zurbuchen and S. K. Streiffer
Materials Science Division, Argonne National Laboratory, Argonne, Illinois 60439

Ferroelectric domain structures of $(001)SrBi_2Nb_2O_9$ epitaxial films, investigated using both transmission electron microscopy and phase-field simulations, are reported. Experiment and numerical simulation both reveal that the domain structures consist of irregularly shaped domains with *curved* domain walls. It is shown that the elastic contribution to domain structures can be neglected in $SrBi_2Nb_2O_9$ due to its small ferroelastic distortion, less than 0.0018%. Two-beam dark-field imaging using reflections unique to domains of each of the two 90° polarization axes reveal the domain structure. Phase-field simulation is based on the elastic and electrostatic solutions obtained for thin films under different mechanical and electric boundary conditions. The effects of ferroelastic distortion and dielectric constant on ferroelectric domains are systematically analyzed. It is demonstrated that electrostatic interactions which favor straight domain walls are not sufficient to overcome the domain wall energy which favors curved domains in $SrBi_2Nb_2O_9$. © *2004 American Institute of Physics.* [DOI: 10.1063/1.1707211]

I. INTRODUCTION

The proper ferroelectrics $SrBi_2Nb_2O_9$ and $SrBi_2Ta_2O_9$ are candidates for use in ferroelectric memory cells due to their extremely high fatigue resistance.[1,2] Although the growth of thin films of these materials has been widely studied, only a few attempts at microstructural characterization have been undertaken,[3–9] and even fewer studies have addressed the ferroelectric domain structure. It is the ferroelectric properties of these materials that are of special technological interest, so study of the domain structures is needed and is expected to provide clues to the origin of their unique behavior.

Recent experimental observations demonstrated that the ferroelectric domain morphology of $SrBi_2Nb_2O_9$ (Ref. 9) and $SrBi_2Ta_2O_9$ (Refs. 10, 11) thin films is irregular, with highly curved domain walls. This differs from prototypical oxide ferroelectrics (e.g., $PbTiO_3$ and $BaTiO_3$), which have high-aspect-ratio domains with crystallographically faceted domain walls. A number of reasons have been proposed to explain the highly faceted and crystallographically restricted ferroelectric domain walls observed in typical oxide ferroelectrics. These include matching of spontaneous strains across walls to minimize elastic distortions, symmetry constraints, intolerance of space charge, and strain arguments.[12–15] In most ferroelectric systems, the axis of remanent polarization is collinear with the axis of greatest ferroelastic distortion from the cubic prototype (e.g., *c* vs *a*), so that experimental determination of the dominant term is frustrated for most systems. One of the unique features of $SrBi_2Nb_2O_9$, however, is the fact that it has almost no ferroelastic distortion; $a = b$ to five significant digits (see Table I). Therefore, in $SrBi_2Nb_2O_9$, the elastic strain component of the free energy balance determining the ferroelectric domain morphology is diminishingly small, smaller than in previously-studied systems by *three orders of magnitude*.

In the present work, we expand upon our initial report[9] on the domain structures in $SrBi_2Nb_2O_9$ by combining dark-field transmission electron microscopy (TEM) observations with computer simulations using the phase-field method. The phase-field approach has previously been applied to modeling microstructural evolution during structural transformations in bulk systems (see, for example, Refs. 23, 24), including domain structure evolution during a ferroelectric phase transition in bulk single crystals.[25–27] The method has been extended to simulate domain structure and its evolution in constrained three-dimensional (3D) ferroelectric thin films,[28–30] where an analytic elastic solution derived for a constrained film having arbitrary eigenstrain distributions and an electrostatic solution derived for a film under different film surface boundary conditions were employed. It was shown that the phase-field approach is able to predict simultaneously the effects of substrate constraint, electrostatic boundary conditions, and temperature on the volume fractions of domain variants, domain wall orientations, domain shapes, and their temporal evolution during a ferroelectric phase transition.

This paper is organized as follows: in Sec. II, the experimental aspects of the work, including the thin film deposition and characterization techniques, are presented. Section III provides a theoretical model based on the phase-field approach. In Sec. IV, the theoretical and experimental results

---

[a)]Author to whom correspondence should be addressed. Electronic mail: yil1@psu.edu

TABLE I. Crystallographic parameters and ferroelastic distortion of some oxide ferroelectrics that have 90° domains at room temperature.

Formula	Unit cell type	Lattice parameters (nm)	Polar axis	Ferroelectric domain morphology	Ferroelastic distortion (%)
$PbTiO_3$	tetragonal	$a = 0.3904$[a] $c = 0.4152$	c	faceted walls high aspect ratio	6.4
$BaTiO_3$	tetragonal	$a = 0.39945$[b] $c = 0.40335$	c	faceted walls high aspect ratio	1.0
$Bi_4Ti_3O_{12}$	monoclinic	$a = 0.54500$[c] $c = 0.54059$	a[e]	faceted walls low aspect ratio[g]	0.82
$SrBi_2Ta_2O_9$	orthorhombic	$a = 0.55306$[d] $c = 0.55344$	a[f]	curved walls granular[h]	0.069
$SrBi_2Nb_2O_9$	orthorhombic	$a = 0.55094(4)$[c] $c = 0.55094(4)$	a[f]	...	<0.0018

[a]Reference 16.
[b]Reference 17.
[c]Reference 18.
[d]Reference 21.
[e]Reference 19.
[f]Reference 22.
[g]Reference 20.
[h]References 10 and 11.

are presented. The degree of influence of ferroelastic distortion and of dielectric constants on the domain morphology is discussed in Sec. V, and conclusions are presented in Sec. VI.

II. EXPERIMENTAL CHARACTERIZATION OF DOMAIN STRUCTURES

Epitaxial $(001)SrBi_2Nb_2O_9$ films were grown on $(001)SrTiO_3$ by pulsed laser deposition, described in detail elsewhere.[31,32] At the growth temperature, the $SrBi_2Nb_2O_9$ epitaxial film is tetragonal and grows with a single orientation relationship to the substrate, $(001)SrBi_2Nb_2O_9 \| (001)SrTiO_3$ and $[100]_{tetragonal}SrBi_2Nb_2O_9 \| [100]SrTiO_3$, shown schematically in Fig. 1(a). On cooling through the transition temperature, however, the a and b axes of $SrBi_2Nb_2O_9$ become distinct through a noncentrosymmetric puckering of the two-

layered $(NbO_6)^{7-}$ octahedral sheets,[33] and the film twins into ferroelectric domains in which either the a or b axis of the room-temperature phase lies parallel to $[110]SrTiO_3$ [we use the A setting of space group $Cmc2_1$ (#36) when discussing the orthorhombic cell of $SrBi_2Nb_2O_9$, so the long axis is the c axis, which is the convention in ferroelectrics]. Views of a unit cell down $[100]$ and $[010]$, shown in Figs. 1(b) and 1(c), demonstrate this graphically. There can be no remanent polarization along c,[5] and the only domain interaction along c is electrostatic, so the $SrBi_2Nb_2O_9$ domain structure is approximately two-dimensional (2D), making it an excellent model system for investigating ferroelectric domain morphology.

Ferroelectric domains were imaged along $[001]$, perpendicular to the plane containing the polar axes. These plan-view TEM samples were prepared by thinning and dimple polishing from the substrate side. After the final mechanical polishing step, specimens were annealed for 5 min at 550 °C in order to cycle through the transition temperature [or Curie point, $T_c \sim 440$ °C (Ref. 34)], renucleate the ferroelectric domains, and alleviate mechanical sample preparation artifacts. Specimens were then argon ion thinned on a liquid nitrogen-cooled stage at 5 kV, at incidence angles from 12° to 20°.

A Philips CM-30 TEM was operated at 100 and 300 kV using a room-temperature sample stage. Kinematically-allowed 120 reflections were used for two-beam dark-field imaging. Simulated $[001]$ electron diffraction patterns of two 90° domains are shown in Fig. 2, with the 120 reflections arrowed in each. The 120 reflection is weak, but the two-beam dark-field technique provides sufficient intensity, and also simplifies image interpretation because the crystal is oriented so that only the planes of interest are strongly diffracting.

Samples were tilted away from the $[001]$ zone axis about the $[210]$ [i.e., parallel to the (120) planes] to a clean two-beam dark field condition, with $s = 0$ to maximize intensity. This required a tilt of about 35° away from the zone axis, due
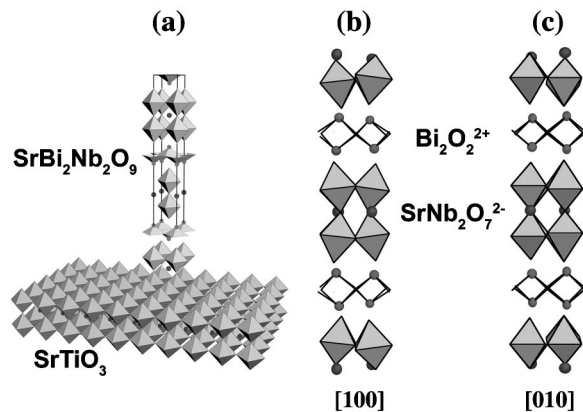

(a)   **(b)**   **(c)**

$SrBi_2Nb_2O_9$

$SrTiO_3$

$Bi_2O_2^{2+}$

$SrNb_2O_7^{2-}$

[100]   [010]

FIG. 1. Schematic of the epitaxial orientation of $SrBi_2Nb_2O_9$ in this study. The tetragonal unit cell, relevant at growth temperature is outlined in (a). (b) and (c) show the orthorhombic unit cell of $SrBi_2Nb_2O_9$ (relevant at room temperature) down the $[100]$ and $[010]$ zone axes, demonstrating the distortions that result in remanent polarization without significant distortion of the lattice parameters.
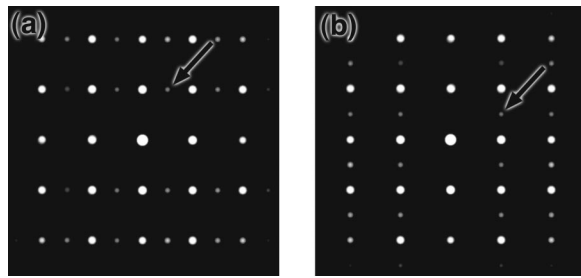
FIG. 2. Simulated [001] zone axis electron diffraction patterns of ortho-rhombic $SrBi_2Nb_2O_9$, showing the location of the 120 reflections (arrowed) for each of the two remanent polarization-axis variants.
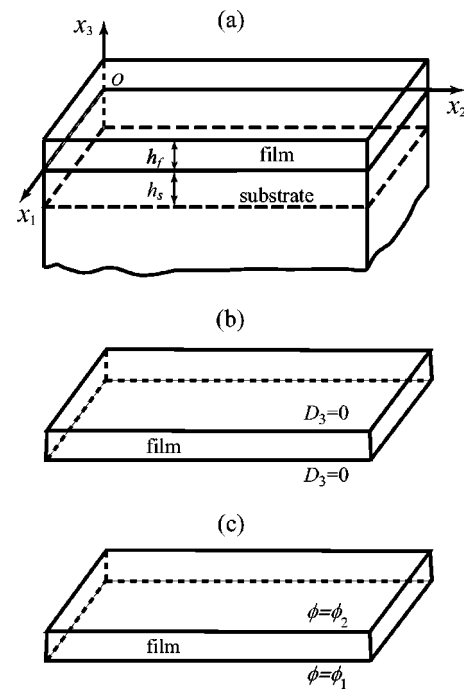

FIG. 3. Schematic illustrations of (a) a thin film coherently constrained by a substrate. The polar axes of the ferroelectric form of $SrBi_2Nb_2O_9$ lie parallel to x_1 and x_2. (b) A film under the electric displacement surface boundary condition; and (c) a film under specified electric potential surface boundary condition.

to the complexity of the crystal structure and the weakness of the 120 reflection. Exposures lasting at least 200 s were required to obtain images with adequate intensity, with exposure times limited by mechanical drift in the instrument.

Images were acquired and processed in a manner that allows visual comparison of the images with a one-to-one spatial correspondence. The large tilt introduced foreshortening in the images, so in order to compare the two 90° ferroelectric domain structures directly, image correction was required. The axis of foreshortening for each image was determined by comparing a rotation-calibrated diffraction pattern and a dark-field image taken at the same two-beam condition. A digital version of the image was then anisotropically stretched until sample-edge features matched those in a [001] zone axis reference image of the same region. A caveat of this technique is that it introduces a *thickness* $\times \sin \theta$ uncertainty (about 10 nm for a typical TEM specimen) in the direction of the foreshortening axis in each image, slightly distorting the appearance of image features. It also causes the images to appear slightly astigmatic.

Sample preparation and TEM work were conducted with extreme care, to avoid altering the domain structure. The final 30 μm of mechanical polishing were conducted using a cloth dimpling tool, rather than the stainless steel tool typically employed. The TEM work in particular was very careful. During tilting, a convergent beam was used to obtain Kikuchi lines as a guide to tilting. In order to minimize beam-sample interactions during this step, a very low beam current (i.e., small spot size) setting was used, and an area near but not coincident with the area of interest was used for tilting in diffraction mode. A liquid nitrogen-cooled stage was used for some work, but these imaging attempts were unsuccessful due to the increased mechanical drift of such stages. The dark-field studies were conducted over a period of several sessions, and the domain structure was not observed to vary with repeated exposures to the electron beam.

It can be argued that this great care taken in preparing and examining TEM samples was not necessary, due to the low influence of elastic strain on ferroelectric domain morphology in this material. In other words, mechanical stresses from sample preparation might be *less* likely to alter the ferroelectric domain structure of $SrBi_2Nb_2O_9$ than for other ferroelectric materials, depending on exactly where in the continuum of elastic interactions $SrBi_2Nb_2O_9$ falls.

III. PHASE-FIELD MODEL

In this section, we describe the phase-field model for predicting domain structures in $SrBi_2Nb_2O_9$ films. We consider the heteroepitaxial $(001)SrBi_2Nb_2O_9$ film with its long tetragonal axis normal to the film/substrate interface as shown in Fig. 1(a). Below the transition temperature, the tetragonal paraelectric phase transforms to a ferroelectric orthorhombic state. The spontaneous polarization is along the a axis of the orthorhombic cell, correspondingly parallel to the [110], [1$\bar{1}$0], [$\bar{1}$10], or [$\bar{1}\bar{1}$0] axis of the high-temperature tetragonal cell. We define an orthogonal coordinate system $x=(x_1,x_2,x_3)$ at the film/substrate interface with x_3 outward normal to the film surface, and x_1 and x_2 along [110] and [$\bar{1}$10] axes of the high-temperature tetragonal cell, respectively [see Fig. 3(a)]. If $\mathbf{P}=(P_1,P_2,P_3)$ is the polarization vector, $(P_1,0,0)$ and $(0,P_2,0)$ describe the ferroelectric orthorhombic variants of $(001)SrBi_2Nb_2O_9$ films in the coordinate system $\mathbf{x}=(x_1,x_2,x_3)$. Therefore, $\mathbf{P}=(P_1,P_2,0)$ describes all possible ferroelectric states in the $(001)SrBi_2Nb_2O_9$ film. The temporal evolution of the polarization field $\mathbf{P}=(P_1,P_2,0)$, and thus the domain structure, is described by the time-dependent Ginzburg–Landau (TDGL) equations,

$$\frac{\partial P_i(\mathbf{x},t)}{\partial t} = -L \frac{\delta F}{\delta P_i(\mathbf{x},t)}, \quad (i=1,2), \tag{1}$$

where L is the kinetic coefficient related to domain-wall mobility, and F is the total free energy of the system. $\delta F/\delta P_i(\mathbf{x},t)$ is the thermodynamic driving force for the spatial and temporal evolution of $P_i(\mathbf{x},t)$.

The total free energy of a film includes the Landau bulk free energy F_{bulk}, domain wall energy F_{wall}, elastic energy F_{elas}, and electrostatic energy F_{elec}, i.e.,

$$F = F_{\text{bulk}}(P_i) + F_{\text{wall}}(P_{i,j}) + F_{\text{elas}}(P_i, \epsilon_{ij}) + F_{\text{elec}}(P_i, E_i)$$

$$= \int \int_V \int [f_{\text{bulk}}(P_i) + f_{\text{wall}}(P_{i,j}) + f_{\text{elas}}(P_i, \epsilon_{ij})$$

$$+ f_{\text{elec}}(P_i, E_i)] d^3x, \tag{2}$$

where V is the volume of the film, $d^3x = dx_1 dx_2 dx_3$, and $P_{i,j} = \partial P_i / \partial x_j$.[35] We assume that the strain field ϵ_{ij} and the electric field E_i are always at equilibrium for a given polarization field distribution, i.e., the elastic strain and electric fields of the film are functions of the polarization field.

A. Landau bulk free energy

We assume that the ferroelectric transition, in the absence of substrate constraint, is first-order, and its bulk thermodynamics is characterized by the Landau free energy

$$f_{\text{bulk}}(P_i) = \alpha_1 (P_1^2 + P_2^2) + \alpha_{11}(P_1^4 + P_2^4) + \alpha_{12} P_1^2 P_2^2$$

$$+ \alpha_{111}(P_1^6 + P_2^6) + \alpha_{112}(P_1^4 P_2^2 + P_1^2 P_2^4), \tag{3}$$

where α_1, α_{11}, α_{12}, α_{111}, and α_{112} are the dielectric stiffness and higher order stiffness coefficients under a stress-free condition. All of the coefficients are assumed to be independent of temperature, except the dielectric stiffness constant α_1, which has a linear temperature (T) dependence based on the Curie–Weiss law,

$$\alpha_1 = \frac{T - \theta}{2\epsilon_0 C}. \tag{4}$$

$\epsilon_0 = 8.85 \times 10^{-12} \, \text{Fm}^{-1}$ is the dielectric permittivity of a vacuum, C is the Curie constant, and θ is the Curie–Weiss temperature.

B. Domain wall energy

There are four variants of the ferroelectric phase, which correspond to the polarization of $(\pm P_s, 0, 0)$ and $(0, \pm P_s, 0)$, respectively. Variants coexist at the cost of adding domain wall energy into the total free energy. In the Ginzburg–Landau model, the domain wall energy can be introduced through gradients of the polarization field,

$$f_{\text{wall}}(P_{i,j}) = \tfrac{1}{2} G_{11}(P_{1,1}^2 + P_{2,2}^2) + G_{12} P_{1,1} P_{2,2} + \tfrac{1}{2} G_{44}(P_{1,2}$$

$$+ P_{2,1})^2 + \tfrac{1}{2} G_{44}'(P_{1,2} - P_{2,1})^2 + \tfrac{1}{2}(G_{44} + G_{44}')$$

$$\times (P_{1,3}^2 + P_{2,3}^2), \tag{5}$$

where G_{ij} are the gradient energy coefficients.

C. Elastic energy

The structural change associated with a proper ferroelectric phase transition is described by stress-free strains, spontaneous strains, or transformation strains. For a given polarization field, the spontaneous strains are calculated by

$$\epsilon_{11}^0 = Q_{11} P_1^2 + Q_{12} P_2^2, \quad \epsilon_{22}^0 = Q_{11} P_2^2 + Q_{12} P_1^2,$$

$$\epsilon_{33}^0 = Q_{13}(P_1^2 + P_2^2), \tag{6}$$

$$\epsilon_{12}^0 = \epsilon_{21}^0 = Q_{44} P_1 P_2, \quad \epsilon_{12}^0 = \epsilon_{21}^0 = 0, \quad \epsilon_{13}^0 = \epsilon_{31}^0 = 0, \tag{7}$$

where Q_{ij} are the electrostrictive coefficients. We assume that the interfaces developed during a ferroelectric phase transition are coherent. Elastic strains e_{ij} will be generated during the phase transition in order to accommodate the structural changes. They are given by

$$e_{ij} = \epsilon_{ij} - \epsilon_{ij}^0, \tag{8}$$

where ϵ_{ij} are the total strains. The corresponding elastic strain energy density can be expressed as

$$f_{\text{elas}}(P_i, \epsilon_{ij}) = \tfrac{1}{2} c_{ijkl} e_{ij} e_{kl} = \tfrac{1}{2} c_{ijkl}(\epsilon_{ij} - \epsilon_{ij}^0)(\epsilon_{kl} - \epsilon_{kl}^0), \tag{9}$$

where c_{ijkl} is the elastic stiffness tensor. The summation convention for the repeated indices is employed and the i, j, k, and l take values of 1, 2, and 3. More details on the calculation of the elastic strain e_{ij} and elastic energy in a film with stress-free surface and constrained by a substrate are available in the literature.[28,29]

D. Electrostatic energy

To consider the dipole–dipole interaction during ferroelectric domain evolution, we calculate the electrostatic energy of a domain structure,

$$f_{\text{elec}}(P_i, E_i) = -\tfrac{1}{2} E_i(\epsilon_0 \kappa_{ij} E_j + P_i), \tag{10}$$

where E_i is the electric field component. The electric displacement D_i is related to the electric field as

$$D_i = \epsilon_0 \kappa_{ij} E_j + P_i, \tag{11}$$

where κ_{ij} is the relative dielectric permittivity of the ferroelectric film.

Suppose there is no space charge inside the film. The electrostatic equilibrium equations of the film can be described by

$$D_{i,i} = 0, \tag{12}$$

with the boundary conditions

$$D_3|_{x_3 = 0, h_f} = 0 \tag{13}$$

for an open-circuit [see Fig. 3(b)], or

$$\phi|_{x_3 = 0} = \phi_1, \quad \phi|_{x_3 = h_f} = \phi_2 \tag{14}$$

if the electric potentials are specified as ϕ_1 on the film bottom surface at $x_3 = 0$ and ϕ_2 on the top surface at $x_3 = h_f$ [see Fig. 3(c)]. h_f is the thickness of the film. ϕ is the electric potential, and

$$E_i = -\phi_{,i}. \tag{15}$$

Combining Eqs. (15), (11), and (12) and assuming $\kappa_{ij} = 0$ when $i \neq j$, the electrostatic equilibrium equation is rewritten as

$$\kappa_{11} \phi_{,11} + \kappa_{22} \phi_{,22} + \kappa_{33} \phi_{,33} = \frac{1}{\epsilon_0}(P_{1,1} + P_{2,2}). \tag{16}$$

In order to solve Eqs. (16), (13) or (16), (14), we let

$$\phi = \phi^A + \phi^B, \tag{17}$$

$$\kappa_{11}\phi^A_{,11} + \kappa_{22}\phi^A_{,22} + \kappa_{33}\phi^A_{,33} = \frac{1}{\epsilon_0}(P_{1,1} + P_{2,2}), \tag{18}$$

$$\kappa_{11}\phi^B_{,11} + \kappa_{22}\phi^B_{,22} + \kappa_{33}\phi^B_{,33} = 0. \tag{19}$$

First, we solve Eq. (18) in 3D space by employing the 3D Fourier transform, i.e.,

$$\phi^A(\mathbf{x}) = \int\int\int_{-\infty}^{+\infty} \hat{\phi}^A(\boldsymbol{\zeta})e^{I\mathbf{x}\cdot\boldsymbol{\zeta}}d^3\zeta, \tag{20}$$

$$\hat{\phi}^A(\boldsymbol{\zeta}) = -\frac{I\zeta_i\hat{P}_i}{\epsilon_0(\kappa_{11}\zeta_1^2 + \kappa_{22}\zeta_2^2 + \kappa_{33}\zeta_3^2)}, \tag{21}$$

$$\hat{P}_i(\boldsymbol{\zeta}) = \frac{1}{(2\pi)^3}\int\int\int_{-\infty}^{+\infty} P_i(\mathbf{x})e^{-I\mathbf{x}\cdot\boldsymbol{\zeta}}d^3x, \tag{22}$$

where $I = \sqrt{-1}$. The next step is to find ϕ^B, in an infinite plate of thickness h_f, satisfying Eq. (19) and the boundary conditions,

$$[-\kappa_{33}\epsilon_0(\phi^A_{,3} + \phi^B_{,3})]|_{x_3=0,h_f} = 0, \tag{23}$$

or

$$(\phi^A + \phi^B)|_{x_3=0} = \phi_1, \quad (\phi^A + \phi^B)|_{x_3=h_f} = \phi_2. \tag{24}$$

We solve the boundary value problem in Eqs. (19), (23) or (19), (24) by employing 2D Fourier transforms. Applying 2D Fourier transform, Eq. (19) becomes

$$\kappa_{33}\frac{d^2\hat{\phi}^B}{dx_3^2} - (\kappa_{11}\zeta_1^2 + \kappa_{22}\zeta_2^2)\hat{\phi}^B = 0, \tag{25}$$

where

$$\hat{\phi}^B(\zeta_1,\zeta_2,x_3)$$
$$= \frac{1}{(2\pi)^2}\int\int_{-\infty}^{+\infty}\phi^B(x_1,x_2,x_3)e^{-I(x_1\zeta_1+x_2\zeta_2)}dx_1dx_2. \tag{26}$$

The solution of Eq. (25) is of the form

$$\hat{\phi}^B(\zeta_1,\zeta_2,x_3) = C_1(\zeta_1,\zeta_2)e^{x_3\sqrt{(\kappa_{11}\zeta_1^2+\kappa_{22}\zeta_2^2)/\kappa_{33}}}$$
$$+ C_2(\zeta_1,\zeta_2)e^{-x_3\sqrt{(\kappa_{11}\zeta_1^2+\kappa_{22}\zeta_2^2)/\kappa_{33}}}. \tag{27}$$

Performing a 2D Fourier transform on the boundary condition Eq. (23) or (24), the unknown coefficients C_1 and C_2 can be determined. Then, we apply the 2D inverse Fourier transform on Eq. (27) and get the solution for ϕ^B, i.e.,

$$\phi^B(x_1,x_2,x_3) = \int\int_{-\infty}^{+\infty}\hat{\phi}^B(\zeta_1,\zeta_2,x_3)e^{I(x_1\zeta_1+x_2\zeta_2)}d\zeta_1d\zeta_2. \tag{28}$$

The sum of solutions A and B, $\phi(\mathbf{x}) = \phi^A(\mathbf{x}) + \phi^B(\mathbf{x})$ gives the solution for the boundary value problem of Eqs.

FIG. 4. [001] selected-area diffraction pattern of the $SrBi_2Nb_2O_9$ film studied by TEM. The superposition of the orthogonal diffraction patterns from the two 90° domain variants leads to an apparent fourfold symmetry. 120 spots unique to the two domain variants are indicated by arrows. Image contrast has been enhanced significantly to show these weak spots; the intensity of major reflections is clipped.

(16), (13) or (16), (14). The total electric field can be calculated by Eq. (15). Consequently, the electrostatic energy can be obtained.

IV. RESULTS

A. Experimental observation of domain structures

A selected-area diffraction pattern of the film is presented in Fig. 4, showing the presence of the 120 reflections from both 90° domain variants. The apparent fourfold symmetry is the result of superposition of the twofold diffraction patterns of the two domains with orthogonal polarization axes, rotated 90° with respect to each other. The 120 reflections used for dark-field imaging are indicated by arrows.

The experimentally determined ferroelectric domain structure is shown in Fig. 5. Bright areas correspond to regions with remanent polarization along the axis indicated by the double arrows (P_s). These are foreshortening-corrected images, so one-to-one spatial comparison of the two images is valid, within the ~10 nm monodirectional uncertainty in each image due to the geometric corrections. Any positional uncertainty due to foil bending is considered to be negligible; the sign of the remanent polarization (180° domains) is not resolved by the technique.

The two domain structures of Fig. 5 are complementary. Bright regions in Fig. 5(a) are dark in Fig. 5(b), and vice versa. Arrows indicate regions where the difference is especially prominent. Close examination, however, reveals that overlap is noticeable in some regions. For example, the area at the bottom right of both images is somewhat bright in both images, but less intense than in other areas. This is, however, entirely reasonable considering the highly irregular nature of the domain structure projected along the viewing axis (the *c* axis), which corresponds to the vertical direction of Figs. 1
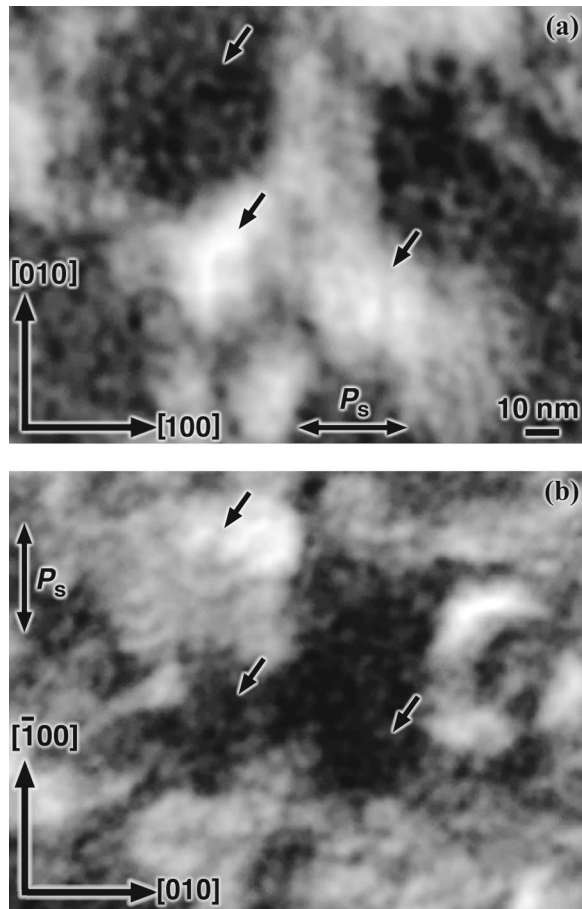
FIG. 5. Two-beam dark-field TEM images of the two 90° ferroelectric domain variants in the SrBi$_2$Nb$_2$O$_9$ film. Comparing the images directly one with another, it is clear that the two domain structures are largely complementary. Bright regions in (a) are dark in (b), and vice versa; especially clear areas are indicated by arrows.
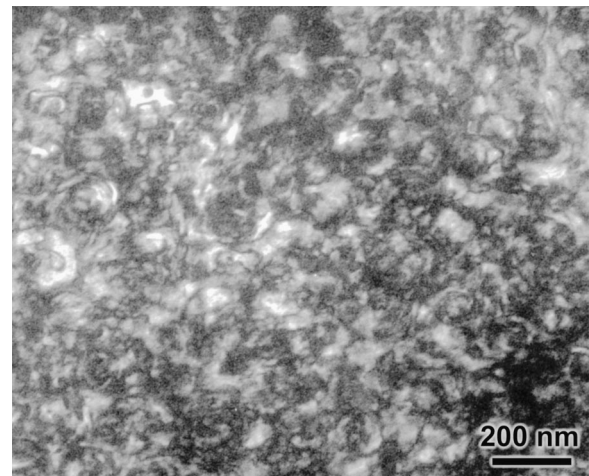

FIG. 6. Two-beam dark-field TEM image of one of the two 90° ferroelectric domain variants in the SrBi$_2$Nb$_2$O$_9$ film, showing that the domain structure does not exhibit faceting or preferred orientations over a large length scale ($>1 \times 1$ μm^2).

and 3 of Ref. 9. The lack of c-axis remanent polarization and the apparent tolerance of space charge by SrBi$_2$Nb$_2$O$_9$ result in some points of a [001] viewing-axis TEM sample containing both types of domains through the foil thickness. Thus, in projection (i.e., a TEM image), a single point may contain contrast from both domain types, resulting in this apparent overlap. These results also agree with the simulated domain structures presented in the next section, for example in Fig. 7(a).

The domain structure on a larger scale is shown in Fig. 6, a dark-field TEM image of one of the two 90° ferroelectric domain types in the same film shown in Figs. 4 and 5. No domain-wall directionality or faceting of the domain structure is apparent in this $>1 \times 1$ μm^2 area. The highly varied and extremely small size of these ferroelectric domains make them very difficult to observe experimentally.

B. Phase-field simulations

In the phase-field simulations, we numerically solve the TDGL Eq. (1) by using the semi-implicit Fourier-spectral method for the time-stepping and spatial discretization.[36] A model size of $128\Delta x \times 128\Delta x \times 36\Delta x$ is employed, with periodic boundary conditions applied along the x_1 and x_2 axes. Δx is the space between any two nearest grid points. The

thickness of the film is taken as $h_f = 20\Delta x$. Suppose the (001)SrBi$_2$Nb$_2$O$_9$ film is grown on (001)SrTiO$_3$ (lattice parameter $a = 0.3905$ nm or $\sqrt{2}a = 0.55225$ nm at room temperature) with a coherent interface. The average constraint strain imposed on the film by the substrate is about $\bar{\epsilon}_{11} = \bar{\epsilon}_{22} = 2.4 \times 10^{-3}$, $\bar{\epsilon}_{12} = 0.0$. We assume the heterogeneous displacements are zero at $x_3 = -h_s = -12\Delta x$ in the substrate. This is because the deformation in the substrate occurs over a distance similar to the film thickness if the heterogeneity in the film is of the order of the film thickness. Previous calculations showed little change in the simulation results when h_s takes a larger value.[29]

The Curie constant and the Curie–Weiss temperature for SrBi$_2$Nb$_2$O$_9$ are taken to be $C = 0.55 \times 10^5$ °C and $\theta = 390$ °C,[34] respectively. The spontaneous polarization arising at the tetragonal to orthorhombic transition temperature is $P_c = 0.148$ C m^{-2} ($P_s = 0.228$ C m^{-2} at room temperature[4]). From these data, the higher-order dielectric stiffness coefficients α_{11} and α_{111} are determined to be[37]

$$\alpha_{11} = -\frac{T_c - \theta}{\epsilon_0 C P_c^2} \tag{29}$$

and

$$\alpha_{111} = \frac{T_c - \theta}{2\epsilon_0 C P_c^4}. \tag{30}$$

In order to ensure that the ferroelectric transition is from tetragonal to orthorhombic, we let the Landau free energy coefficients $\alpha_{12} = -10\alpha_{11}$ and $\alpha_{112} = 2\alpha_{111}$.

We choose the gradient energy coefficients as $G_{11}/G_{110} = 1.2$, $G_{12}/G_{110} = 0.0$, and $G_{44}/G_{110} = G'_{44}/G_{110} = 0.6$. At $T = 25$ °C, the width of a domain wall is about $2.5\Delta x$. If $\Delta x = l_0$, $l_0 = \sqrt{G_{110}/\alpha_0}$, and $\alpha_0 = |\alpha_1|_{T = 25 °C}$, the domain wall energy density is evaluated to be about $1.48\alpha_0 l_0 P_s^2$ for 90° domain walls. Suppose $l_0 = 1.0$ nm, then $G_{110} = 3.75 \times 10^{-10}$ C^{-2} m^4 N, and the corresponding domain wall energy density is about 0.0289 N m^{-1}.

(a)   (b)
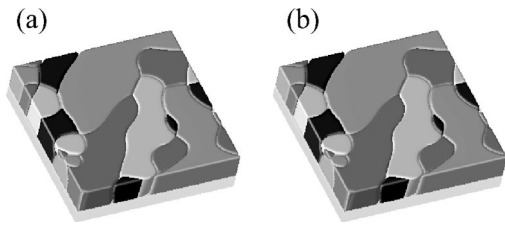

FIG. 7. Simulated domain structure of a $SrBi_2Nb_2O_9$ film dictated by Laudau free energy and gradient energy, (a) with elastic energy; (b) without elastic energy. Shading represents the polarization direction in these and all subsequent simulation results: white=$(P_1,0,0)$, light gray=$(-P_1,0,0)$, dark gray=$(0,P_2,0)$, and black=$(0,-P_2,0)$.

(a)   (b)

FIG. 8. Simulated domain structure of a $SrBi_2Nb_2O_9$ film dictated by Laudau free energy and gradient energy, and electric energy with $\kappa=190$ under (a) short-circuit $\phi_0=0$ and (b) open-circuit $D_3=0$ conditions, respectively.

Initially, we simulated the effect of the elastic energy resulting from the ferroelectric phase transition and the substrate constraint on the domain structure in the $SrBi_2Nb_2O_9$ film. Because experimental data for the elastic constants of $SrBi_2Nb_2O_9$ are not available in the literature, we assumed that $SrBi_2Nb_2O_9$ is elastically isotropic, and the Young's modulus and Poisson's ratio are taken to be $E=2.87 \times 10^{11}\,\mathrm{N\,m^{-2}}$ and $\nu=0.31$, respectively. Our previous simulations of the domain structures of $PbTiO_3$ films showed no significant difference by assuming cubic or isotropic elasticity.[28,29] Similar isotropic assumption of the dielectric constants was made when we considered the dipole–dipole interaction. The elastic tensor components are calculated through $c_{ijkl}=\lambda\,\delta_{ij}\delta_{kl}+\mu\,\delta_{ik}\delta_{jl}+\mu\,\delta_{il}\delta_{jk}$, $\lambda=2\mu\nu/(1-2\nu)$, and $E=2(1+\nu)\mu$. Based on the spontaneous strain of $SrBi_2Nb_2O_9$ being $\sim 2.0\times10^{-5}$, we set $Q_{11}=0.385 \times10^{-3}\,\mathrm{C^{-2}\,m^4}$, $Q_{13}=0.0$, $Q_{12}=-0.04\times10^{-3}\,\mathrm{C^{-2}\,m^4}$, and $Q_{44}=0.05\times10^{-3}\,\mathrm{C^{-2}\,m^4}$. We started the simulation from a homogeneous paraelectric phase created by assigning a zero value at each grid point for each component of the polarization field plus a small random noise of uniform distribution. The simulation results are shown in Fig. 7 where the electrostatic energy was not taken into account. In this and all simulation figures, the white and light gray shaded regions represent domains consisting of type $(P_1,0,0)$ and $(-P_1,0,0)$, respectively; and dark gray and black shading indicate domains of type $(0,P_2,0)$ and $(0,-P_2,0)$, respectively. The domain morphology is represented by contours of $P_i^* =|P_i|/P_s=0.6$. It can be seen that the ferroelectric domains have irregular shapes and the domain walls are highly curved, in excellent agreement with experimental observations. The domain structure in Fig. 7(a) was obtained from a simulation including the contribution of elastic energy. It is almost exactly the same as that in Fig. 7(b) where only the Landau free energy and the domain wall energy were considered. The two domain structures were obtained from the same initial noise distribution. The results in Fig. 7 indicate that the contribution of the elastic energy to the domain morphology of $SrBi_2Nb_2O_9$ film is insignificant. This is a result of the diminishingly small lattice mismatch among the domains.

In the above simulations, electrostatic interactions are ignored. Although the elastic energy contribution is insignificant, the question remains whether or not the electrostatic i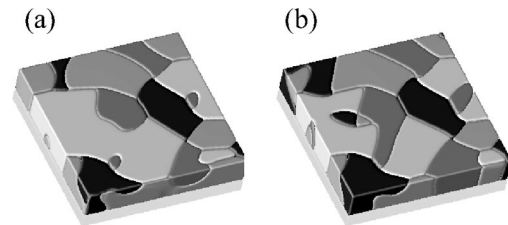nteractions which also would favor straight domain walls are sufficient to result in faceted domains. Therefore, we also incorporated the electrostatic energy contribution. In the simulation, the dielectric constants were taken as $\kappa_{11}=\kappa_{22} =\kappa_{33}=\kappa=190$, from bulk crystal values.[34] Experimental measurements indicate that $SrBi_2Nb_2O_9$ films have a dielectric constant similar to that of the bulk crystal.[3,4,38] The open-circuit electric boundary condition, Eq. (13), and short-circuit electric boundary condition, Eq. (14) at $\phi_1=\phi_2 =\phi_0$ are considered, respectively. The corresponding domain structures from both electric boundary conditions shown in Figs. 8(a) and 8(b) have a similar morphology, i.e., irregular domain shapes with curved domain walls. The electric surface boundary condition does not significantly affect the domain structure, largely due to the fact that the polarization is parallel to the film surface (completely in the plane of the film) and the film is very thin.

V. DISCUSSION

Both our experimental observations and phase-field simulations show that the $SrBi_2Nb_2O_9$ exhibits curved domain walls. When visually comparing the domain morphology of simulation and experiment, it is important to keep in mind that experiment does not resolve 180° domains. Thus, regions in simulated images that are white and light gray appear as single contiguous regions in experimental images, and likewise for dark gray and black regions. Judging from the simulated domain structures, it appears likely that regions of high negative curvature in experimental images are associated with 180° domain boundaries.

There are mainly three factors that control the domain morphology and the domain wall orientations: the domain wall energy anisotropy, anisotropic elastic interactions, and electrostatic interactions. An isotropic domain wall energy contribution favors spherical domains with curved domain walls. The minimum elastic energy is achieved if the domain walls are oriented along directions such that the neighboring domains are lattice-matched across the domain walls. Electrostatic energy minimization leads to straight domain walls with no local space charge.

In a given system, the domain morphology and domain wall orientations are determined by a balance among the three factors. For example, if we increase the values of the electrostrictive coefficients, Q_{ij}, the effect of the elastic energy becomes increasingly important. It can be seen from Figs. 9(a) and 9(b), where Q_{ij} were increased 500 and 1000 times, respectively. The domain walls become increasingly
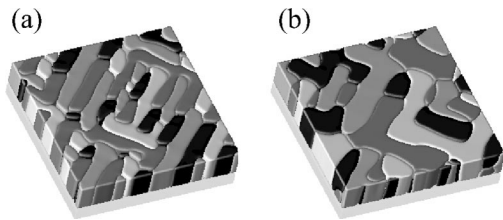
FIG. 9. Simulated domain structure obtained by using larger electrostrictive coefficients, greater than in SrBi$_2$Nb$_2$O$_9$ by (a) $Q_{11}=0.385$, $Q_{12}=-0.04$, $Q_{44}=0.05$; and (b) $Q_{11}=0.193$, $Q_{12}=-0.02$, $Q_{44}=0.025$.

faceted with increasing Q_{ij}, developing a preferred orientation. A plot of domain morphology vs Q_{11} and Q_{12} is summarized in Fig. 10 for fixed values $Q_{13}=0.0$ and $Q_{44}=0.05$. The dashed line represents the isotropic expansion with zero distortion. Simulated domain morphologies and their corresponding symbols in the plot in Fig. 10(a) are given in Figs. 10(b) and 10(c). It can be seen that domain morphology does not change much with differing volume expansion within the approximation of isotropic elastic modulus, but it varies significantly with ferroelastic distortion, even in the case of isotropic elasticity. When the distortion is large the domains are faceted with higher aspect ratios.

In the particular system, SrBi$_2$Nb$_2$O$_9$, the elastic energy contribution is so small that it can be neglected, as shown in our simulations. We also show that even if the electrostatic energy which favors straight domain walls is included in the simulations, it is not sufficiently large to make the domain walls straight in SrBi$_2$Nb$_2$O$_9$. That is, the isotropic domain wall energy dominates the domain morphology. For systems with smaller dielectric constant, the contribution of electrostatic energy becomes increasingly important. For example, Fig. 11 shows simulated domain morphologies with varying dielectric constant, $\kappa=20$, 190, 1000, and 4000 under the open-circuit electric boundary condition. It is easy to see that small dielectric constant, i.e., large electrostatic energy, can also result in domain wall faceting [see Fig. 11(a), $\kappa=20$]. The effect of electrostatic energy on the domain morphology is diminished for larger dielectric constants. When $\kappa=4000$, the effect of the electrostatic energy on the domain morphology can be ignored.

VI. CONCLUSIONS

The 90° ferroelectric domain structure of SrBi$_2$Nb$_2$O$_9$ was investigated by dark-field TEM and by phase-field simulation. Both experiment and simulation showed that ferroelectric domain walls in SrBi$_2$Nb$_2$O$_9$ are highly curved, and that the domain shapes are irregular due to the low ferroelastic distortion of SrBi$_2$Nb$_2$O$_9$. The effect of ferroelastic distortion on the domain shapes was systematically modeled, and it was shown that domain walls become increasingly faceted as the ferroelastic distortion is increased. Our computer simulations also demonstrate that domain walls become increasingly faceted as the dielectric constant is decreased.

These results imply that the faceted nature of prototypical oxide ferroelectrics is primarily the result of ferroelastic
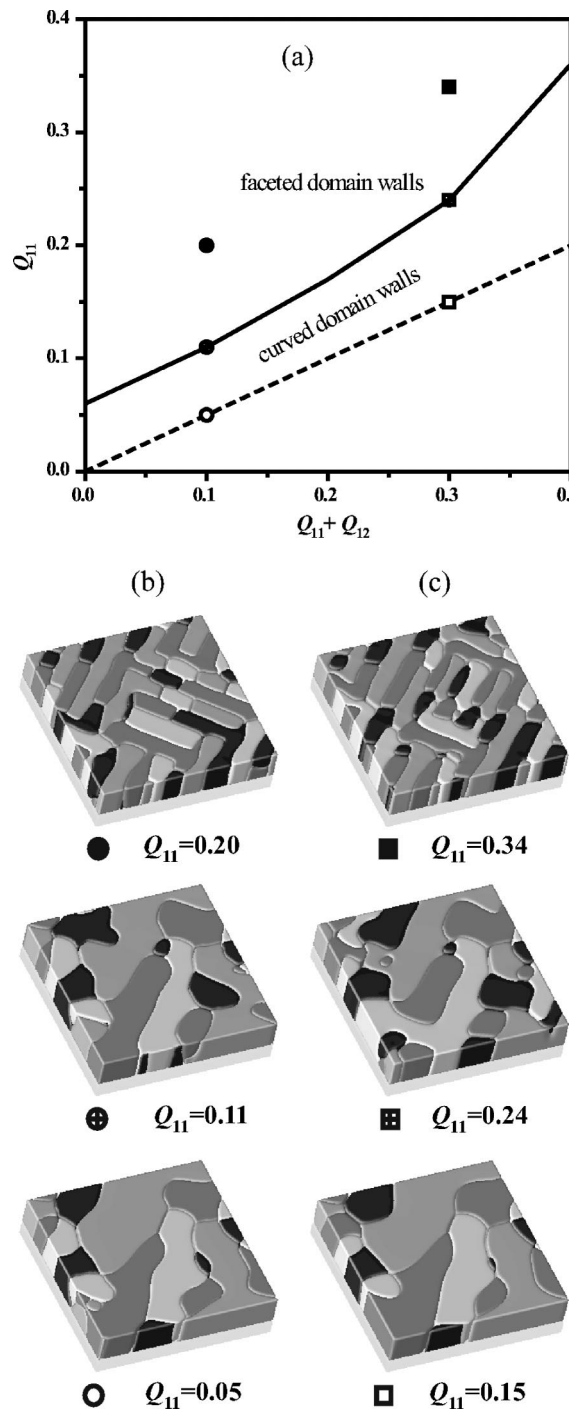

FIG. 10. (a) Domain morphology diagram vs electrostrictive coefficients Q_{11} and Q_{12}; domain structures with (b) $Q_{11}+Q_{12}=0.1$ and (c) $Q_{11}+Q_{12}=0.3$.

distortions (strain energy minimization). These results may have implications for efforts to understand the fatigue-resistance of SrBi$_2$Nb$_2$O$_9$, SrBi$_2$Ta$_2$O$_9$, and perhaps for the search for other fatigue-free ferroelectrics. Further study of low-distortion and low-fatigue systems should help to reveal correlations. In particular, experimental investigation of the ferroelectric domain structure of other ferroelectric materials having a high κ, but slightly larger ferroelastic distortion may lead to the discovery of other oxide ferroelectrics with reduced geometric constraints on domain walls. Study of a
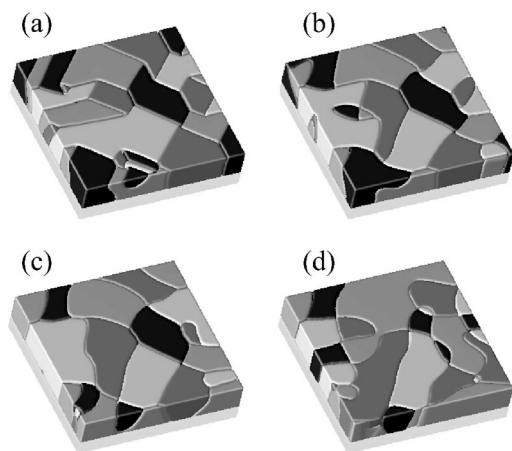
FIG. 11. The effect of dielectric constant on domain structure, as dictated by Laudau free energy, gradient energy, and electric energy under the open-circuit condition, (a) $\kappa=20$; (b) $\kappa=190$; (c) $\kappa=1000$; (d) $\kappa=4000$.

low κ, low-distortion ferroelectric would be a valuable experimental test of the theoretical predictions presented here. Studies of these domain structures using an uncharged probe, x rays, are also planned.

[1] C. A. Paz de Araujo, J. D. Cuchiaro, L. D. McMillan, M. C. Scott, and J. F. Scott, Nature (London) **374**, 627 (1995).
[2] T. Sumi, Y. Judai, K. Hirano, T. Ito, T. Mikawa, M. Takeo, M. Azuma, S. Hayashi, Y. Uemoto, K. Arita, T. Nasu, Y. Nagano, A. Inoue, A. Matsuda, E. Fuji, Y. Shimada, and T. Otsuki, Jpn. J. Appl. Phys., Part 1 **35**, 1516 (1996).
[3] J. Lettieri, M. A. Zurbuchen, Y. Jia, D. G. Schlom, S. K. Streiffer, and M. E. Hawley, Appl. Phys. Lett. **76**, 2937 (2000).
[4] J. Lettieri, M. A. Zurbuchen, Y. Jia, D. G. Schlom, S. K. Streiffer, and M. E. Hawley, Appl. Phys. Lett. **77**, 3090 (2000).
[5] M. A. Zurbuchen, J. Lettieri, Y. Jia, D. G. Schlom, S. K. Streiffer, and M. E. Hawley, J. Mater. Res. **16**, 489 (2001).
[6] M. A. Zurbuchen, J. Lettieri, S. K. Streiffer, Y. F. Jia, M. E. Hawley, X. Q. Pan, A. H. Carim, and D. G. Schlom, Integr. Ferroelectr. **33**, 27 (2001).
[7] T. Suzuki, Y. Nishi, M. Fujimoto, K. Ishikawa, and H. Funakubo, Jpn. J. Appl. Phys., Part 2 **38**, L1265 (1999).
[8] K. Ishikawa, H. Funakubo, K. Saito, T. Suzuki, Y. Nishi, and M. Fujimoto, J. Appl. Phys. **87**, 8018 (2000).
[9] M. A. Zurbuchen, G. Asayama, D. G. Schlom, and S. K. Streiffer, Phys. Rev. Lett. **88**, 107601 (2002).
[10] Y. Ding, J. S. Liu, and Y. N. Wang, Appl. Phys. Lett. **76**, 103 (2000).
[11] X. H. Zhu, J. M. Zhu, S. H. Zhou, Q. Li, Z. G. Liu, and N. B. Ming, Appl. Phys. Lett. **78**, 799 (2001).
[12] F. Jona and G. Shirane, *Ferroelectric Crystals* (Pergamon, Oxford, 1962).
[13] E. Fatuzzo and W. J. Merz, *Ferroelectricity* (North–Holland, Amsterdam, 1967).
[14] M. E. Lines and A. M. Glass, *Principles and Applications of Ferroelectrics and Related Materials* (Clarendon, Oxford, 1977).
[15] J. F. Scott, Ferroelectr. Rev. **1**, 1 (1998).
[16] *Landolt-Börnstein: Numerical Data and Functional Relationships in Science and Technology*, edited by K.-H. Hellwege and A. M. Hellwege (Springer-Verlag, Berlin, 1981), Vol. 16a, p. 360, Group III (New Series).
[17] J. Harada, T. Pederson, and Z. Barnea, Acta Crystallogr., Sect. A: Foundations of Crystallography **26**, 336 (1970).
[18] A. D. Rae, J. G. Thompson, R. L. Withers, and A. C. Willis, Acta Crystallogr., Sect. B: Struct. Sci. **46**, 474 (1990).
[19] Polarization lies almost entirely along a^* (8% along c). S. E. Cummins and L. E. Cross, J. Appl. Phys. **39**, 2268 (1968).
[20] Y. Barad, J. Lettieri, C. D. Theis, D. G. Schlom, J. C. Jiang, and X. Q. Pan, Appl. Phys. Lett. **89**, 1387 (2001).
[21] A. D. Rae, J. G. Thompson, and R. L. Withers, Acta Crystallogr., Sect. B: Struct. Sci. **48**, 418 (1992).
[22] *International Tables for Crystallography, Vol. A: Space-Group Symmetry*, edited by T. Hahn (Kluwer Academic, Dordrecht, 1996), p. 783.
[23] Y. Z. Wang and L. Q. Chen, in *Method in Materials Research*, edited by E. N. Kaufmann (Wiley, New York, 2000).
[24] L. Q. Chen, "Phase-field Models for Microstructure Evolution", Annual Review of Materials Research 32, 113-140 (2002).
[25] S. Nambu and D. A. Sagala, Phys. Rev. B **50**, 5838 (1994).
[26] H. L. Hu and L. Q. Chen, J. Am. Ceram. Soc. **81**, 492 (1998).
[27] S. Semenovskaya and A. G. Khachaturyan, J. Appl. Phys. **83**, 5125 (1998).
[28] Y. L. Li, S. Y. Hu, Z. K. Liu, and L. Q. Chen, Appl. Phys. Lett. **78**, 3878 (2001).
[29] Y. L. Li, S. Y. Hu, Z. K. Liu, and L. Q. Chen, Acta Mater. **50**, 395 (2002).
[30] Y. L. Li, S. Y. Hu, Z. K. Liu, and L. Q. Chen, Appl. Phys. Lett. **81**, 427 (2002).
[31] J. Lettieri, Y. Jia, M. Urbanik, C. I. Weber, J. P. Maria, D. G. Schlom, H. Li, R. Ramesh, R. Uecker, and P. Reiche, Appl. Phys. Lett. **73**, 2923 (1998).
[32] J. Lettieri, Y. Jia, S. J. Fulk, D. G. Schlom, M. E. Hawley, and G. W. Brown, Thin Solid Films **379**, 64 (2000).
[33] R. E. Newnham, R. W. Wolfe, and J. F. Dorrian, Mater. Res. Bull. **6**, 1029 (1971).
[34] *Landolt–Börnstein: Numerical Data and Functional Relationships in Science and Technology*, edited by K.-H. Hellwege and A. M. Hellwege (Springer-Verlag, Berlin, 1981), Vol. 16a, p. 233, Group III (New Series).
[35] The comma in the subscript indicates that the partial derivative is to be taken with respect to the spatial coordinate index that follows the comma. For example, $\phi_{,i}=\partial\phi/\partial x_i$, $\phi_{,11}=\partial^2\phi/\partial x_1^2$, and $D_{i,i}=(\partial D_1/\partial x_1)+(\partial D_2/\partial x_2)+(\partial D_3/\partial x_3)$. This notation is used throughout this paper.
[36] L. Q. Chen and J. Shen, Comput. Phys. Commun. **108**, 147 (1998).
[37] M. J. Haun, E. Furman, S. J. Jang, H. A. McKinstry, and L. E. Cross, J. Appl. Phys. **62**, 3331 (1987).
[38] $\kappa_{33}=175\pm5$. This was measured on an epitaxial $(001)SrBi_2Nb_2O_9/(001)(La,Sr)_2CuO_4/(001)SrTiO_3$ film at a measurement frequency of 1 kHz. J. Lettieri, Y. Jia, C. I. Weber, D. G. Schlom, H. Li, R. Ramesh, G. W. Brown, M. E. Hawley, R. Uecker, and P. Reiche, presented at the 5th International Workshop on Oxide Electronics, College Park, MD, 1998 (unpublished).